

Article

A Stress-Induced Martensitic Transformation in Aged $\text{Ti}_{49}\text{Ni}_{51}$ Alloy after High-Velocity Impact

Yingying Zhu, Haizhen Wang, Zhiyong Gao * and Wei Cai

Science and Technology on Materials Performance Evaluation in Space Environment Laboratory, School of Materials Science and Engineering, Harbin Institute of Technology, Harbin 150001, China; zhuyingying841225@163.com (Y.Z.); sleepsid@163.com (H.W.); waicai@hit.edu.cn (W.C.)

* Correspondence: sma@hit.edu.cn; Tel.: +86-451-8641-8649

Academic Editor: Martin O. Steinhauser

Received: 4 May 2016; Accepted: 16 June 2016; Published: 23 June 2016

Abstract: The effects of a high-velocity impact on the microstructure, phase transformation and mechanical property of aged $\text{Ti}_{49}\text{Ni}_{51}$ alloy are investigated. The transformation behavior and microstructure along the impact direction after impact emerge with regionalization characteristics, including a deformed region near the crater (0–4 mm) and an un-deformed region of the distal crater (5–6 mm). Stress-induced martensite is the main deformation mechanism in the deforming region of aged $\text{Ti}_{49}\text{Ni}_{51}$ alloy under high-velocity impact.

Keywords: aged $\text{Ti}_{49}\text{Ni}_{51}$ alloy; microstructure; martensitic transformation; high-velocity impact; regionalization characteristics

1. Introduction

TiNi shape memory alloys (SMA) have many current and potential engineering applications since their shape memory and superelasticity properties relate to the martensitic transformation induced by thermal or stress [1–3]. In aeronautics and astronautics applications, SMA devices would suffer a high-velocity impact from space debris, which often results in a change in the transformation behavior and microstructures [4,5].

As we know, aging treatment is an effective technology to adjust a material's performance [6]. The aging of Ni-rich TiNi alloy can lead to the precipitation of Ti_3Ni_4 , Ti_2Ni_3 and TiNi_3 precipitates. Ti_3Ni_4 is coherent with the matrix B2 and is the most influential in affecting the transformation behavior. Unlike fully annealed and quenched near-equiatom TiNi alloys, which transform from B2 to B19' directly, aged Ni-rich TiNi alloys normally transform in two stages (B2-R-B19') [7–9].

Liu investigated the shock-induced transformation behavior in NiTi SMA, and a three-step reverse phase transformation was observed [10]. Kurita et al. studied the transformation behavior of shock-compressed $\text{Ni}_{48}\text{Ti}_{52}$; a one-step transformation was observed before the shock treatment, and a three-step transformation was also found after annealing at an appropriate temperature on the shock-treated $\text{Ni}_{48}\text{Ti}_{52}$ [11]. The appearance of a three-step phase transformation may be because the shock wave makes the energy difference between the grain interior and grain boundary increase, and this results in the desynchronization of the phase transformation process.

The above research is conducted on the transformation behavior and microstructures of solution-treated TiNi alloys. So far, the research of high-velocity impact on aged $\text{Ti}_{49}\text{Ni}_{51}$ alloy is still in blank. In this paper, the transformation behavior and deformed microstructures in aged $\text{Ti}_{49}\text{Ni}_{51}$ alloys under high-velocity impact are characterized to investigate the deformed microstructure evolution from the crater rim to the matrix.

2. Materials and Methods

Ti₄₉Ni₅₁ shape memory alloy rod was hot-forged at 1173 K by Beijing Shape Memory Company (Beijing, China). Specimens with 17.5 mm diameter and 12 mm thickness were cut from the rod using a spark-erosion cutting machine. All the sealed samples were solution treated at 1173 K for 2 h and water-quenched to obtain a supersaturated homogeneous solid solution, and then aged at 773 K for 1 h.

Impact experiments were carried out on a powder gun, with a schematic diagram of the powder gun equipment shown in Figure 1a. A GCr15 steel ball with a 3 mm diameter was used as a projectile with the distance between the target and gun barrel being ~10 cm. The impact velocity was measured using a magnetic instrument [12] and a muzzle velocity of ~1.03 km·s⁻¹ was obtained.

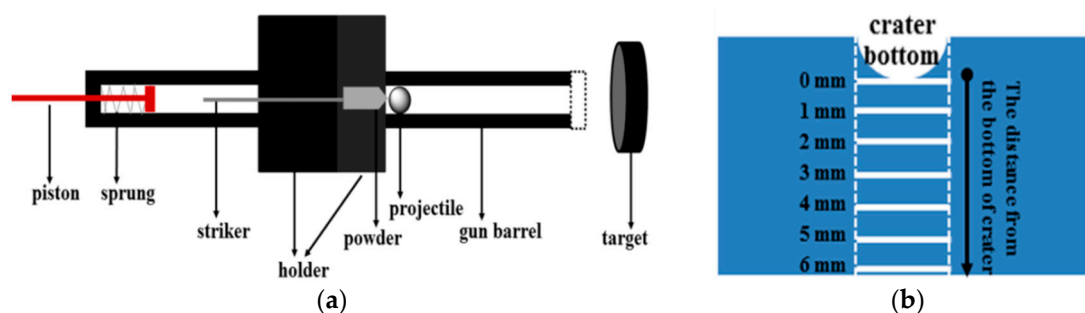


Figure 1. Schematic diagram of the powder gun equipment (a) and sampling modes of DSC and TEM specimens (b) [13].

After impact, aged Ti₄₉Ni₅₁ alloy specimens were cut in a longitudinal direction using a spark-erosion cutting machine and polished mechanically. As shown in Figure 1b, thin sheets (represented by white lines) on the edge of the crater along the impact direction were cut and examined by differential scanning calorimetry (DSC, Perkin Elmer Diamond, New York, NY, USA) at 20 K·min⁻¹ from 373 K to 193 K, the sample was heated from room temperature to 373 K, kept for 1 min, then cooled to 193 K, kept 1 min, and then heated to 373 K. Transmission electron microscopy (TEM) studies were carried out using a Philips CM-12 microscope (FEI, Rotterdam, The Netherlands) at 120 kV to observe the sample microstructure. Vickers hardness measurements were conducted using 300 g loads for a loading time of 15 s using a MMT-3 microhardness tester (Matsuzawa, Tokyo, Japan). Samples used for hardness measurement were ground and polished.

3. Results and Discussion

3.1. Transformation Behavior

Figure 2 shows the DSC curves of aged Ti₄₉Ni₅₁ alloy specimens after impact during two thermal cycles with different distances (0–6 mm) from the bottom of the crater. A one-step phase transformation occurs corresponding to B2↔B19' for solution-treated Ti₄₉Ni₅₁ alloy in Figure 2a. The DSC curves of the aged Ti₄₉Ni₅₁ sample before impact are shown in Figure 2b, and it can be seen that multi-step phase transformation occurs compared with the solution-treated Ti₄₉Ni₅₁ alloy. This clearly shows that peak 5 and peak 1 are a pair of phase transformation. They may show a B19'↔B2 transformation in the grain interior, where Ti₃Ni₄ particles are essentially free. The cooling peak 4 corresponds to its reverse transformation peak 2, which occurs in the grain boundary region. As this pair of peaks has only a narrow hysteresis of 2 K, we can deduce that it may be a B2→R transformation and its reverse transformation. From the microstructure of this sample, as shown in Figure 3a, which shows a segregation of Ti₃Ni₄ particles around the grain boundaries, we can identify that peak 4 and peak 2 correspond, respectively, to the R phase transformation and its reverse transformation of the grain boundary regions. In addition, peak 6 and peak 3 are a pair of phase transformation, and they may show a R↔B19' transformation at the grain boundary region, as the R phase transformation occurs

only in the presence of Ti_3Ni_4 particles [14]. As Fan et al. pointed out, the occurrence of a three-step martensitic transformation for aged TiNi alloy depends on the distribution of Ti_3Ni_4 particles between the grain interior and grain boundary [15].

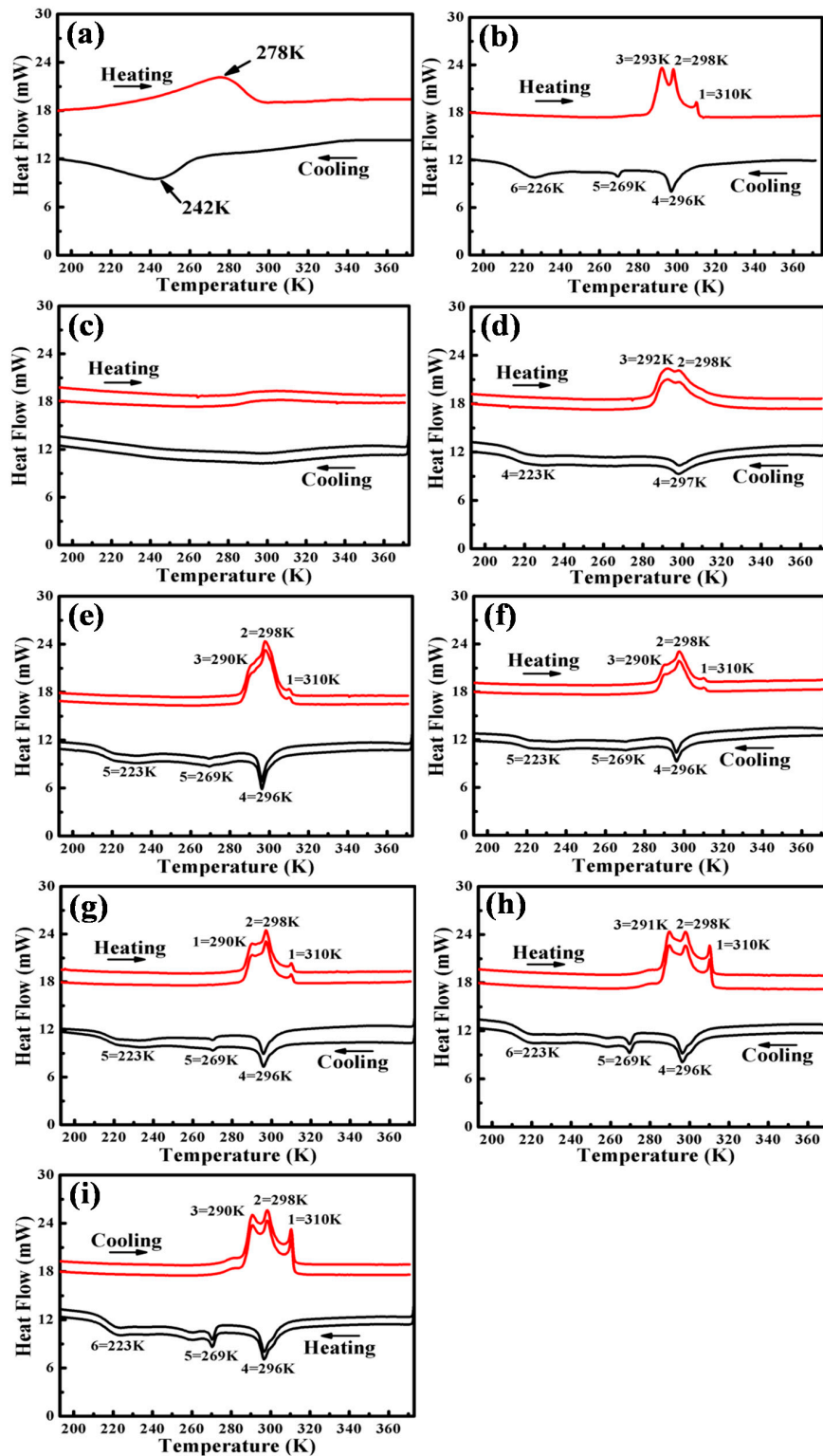


Figure 2. DSC curves for aged $Ti_{49}Ni_{51}$ alloy with different distances (0–6 mm) from the crater before and after impact: (a) solution-treated; (b) non-impact; (c) 0 mm; (d) 1 mm; (e) 2 mm; (f) 3 mm; (g) 4 mm; (h) 5 mm; (i) 6 mm.

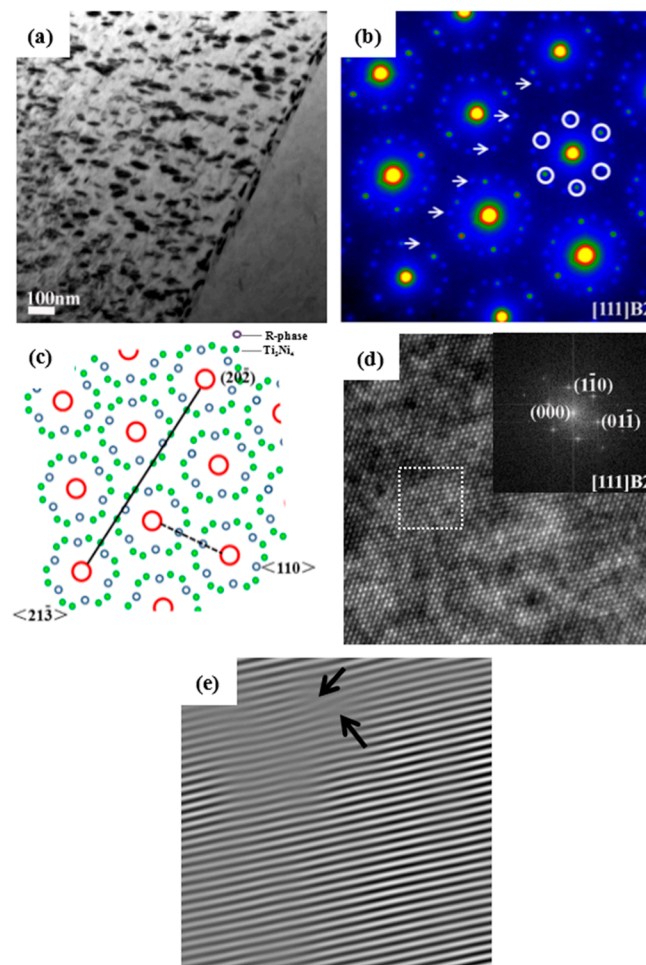


Figure 3. TEM micrographs and SAED patterns of aged $\text{Ti}_{49}\text{Ni}_{51}$ alloy before impact: (a) Bright-field image; (b) SAED pattern; (c) Corresponding schematic representation of (b); (d) High-resolution TEM image of (a); (e) Inverse Fourier filtered image of the area indicated by a dotted square in (d).

The DSC curves of impacted $\text{Ti}_{49}\text{Ni}_{51}$ alloy are presented in Figure 2c–i. On the bottom of the crater (0 mm), the exothermic and endothermic peaks are too wide to be observed in the range of from 193 K to 373 K. As the distance is 1 mm, two endothermic peaks (peak 2 and peak 3) before impact partially overlap after impact, and this may be because the stress concentrated in the grain boundary during the high-velocity impact, and the stress-induced martensite phase transformation happens while, at the same time, the uneven distribution of stress leads to the width and overlap of peak 2 and peak 3 [16]. The exothermic and endothermic peaks become sharper gradually with the increasing distance (2–4 mm), as shown in Figure 2d–g; meanwhile, peak 3 and peak 2 separated gradually due to less deformation. As the distance is 5–6 mm, the exothermic and endothermic peaks in Figure 2h,i are quite similar to the transformation behavior before impact treatment (Figure 2b).

3.2. Deformed Microstructure

Figure 3 shows the TEM micrographs and the selected area electron diffraction (SAED) pattern of aged $\text{Ti}_{49}\text{Ni}_{51}$ alloy. Aged $\text{Ti}_{49}\text{Ni}_{51}$ alloy exhibits finely dispersed Ti_3Ni_4 particles embedded in the grain interior (Figure 3a). The SAED pattern is shown Figure 3b, and it should be noticed that the microstructures are B2 austenite, R phase corresponding to $1/3 \langle 110 \rangle$ B2 super-lattice spots marked with some white circles, and Ti_3Ni_4 particles corresponding to $1/7 \langle 213 \rangle$ B2 super-lattice spots marked with some white arrows [17]. The corresponding schematic representation is shown in Figure 3c

(blue circles represent the R phase, green circles represent Ti_3Ni_4 particles). Moreover, the dislocation density is approximately calculated to be $8.90 \times 10^{11} \text{ cm}^{-2}$ according to the high-resolution TEM image in Figure 3d,e.

The TEM and SAED patterns of $\text{Ti}_{49}\text{Ni}_{51}$ alloys on the bottom (0 mm) of the crater after impact are shown in Figure 4a–c; a lot of plates appear in Figure 4a, and from the SAED pattern in Figure 4b, the structure of the martensite plates is B19'. Meanwhile, the parent phase, R phase, and Ti_3Ni_4 particles were found in Figure 4c. According to the high-resolution TEM image in Figure 4d,e, the dislocation density is approximately calculated to be $1.40 \times 10^{12} \text{ cm}^{-2}$, which is no significant increase compared with of the density before impact.

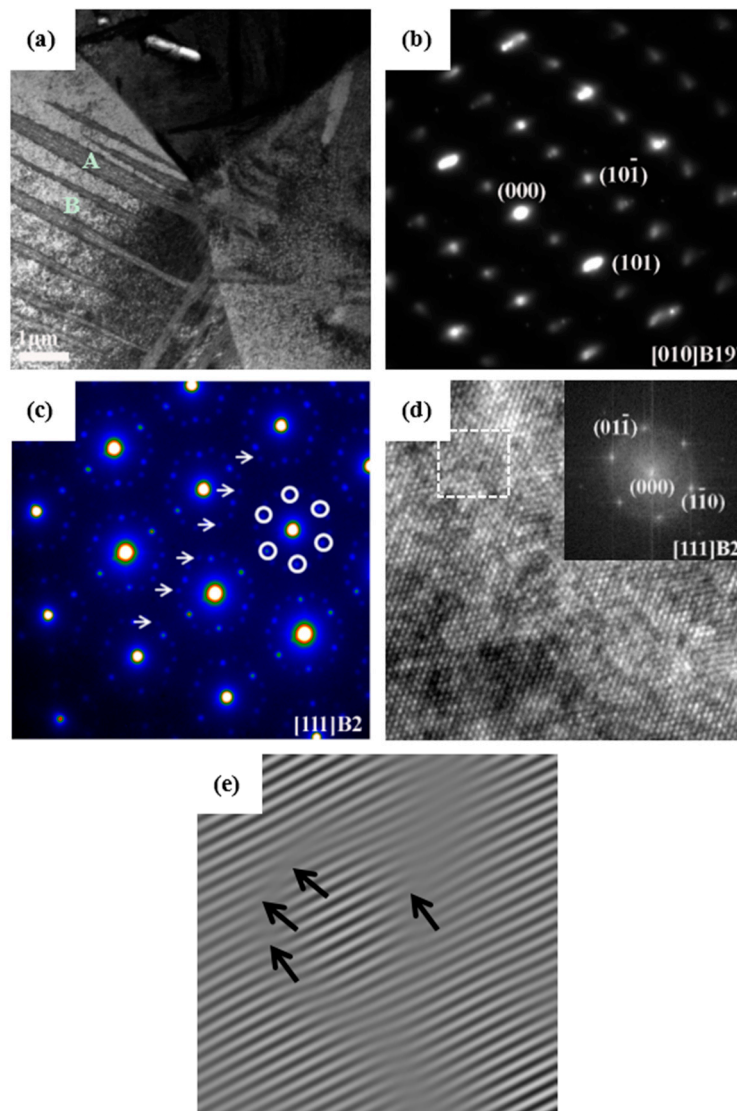


Figure 4. TEM micrographs and SAED patterns of aged $\text{Ti}_{49}\text{Ni}_{51}$ alloy after impact: (a) Bright-field image of the bottom of crater (0 mm); (b) SAED pattern of area A in (a); (c) SAED pattern of area B in (a); (d) High-resolution TEM image of (a); (e) Inverse Fourier filtered image of the area indicated by a dotted square in (d).

From Figure 4a, the martensite plate begins to nucleate in the grain boundary region, and this may be because the shock treatment increases the non-chemical free energy such as the strain energy and interfacial energy of the grain boundary, which provide part of the driving force for nucleation

and the growth of martensite; as a result, a martensite plate grows from the grain boundary to the grain interior. Partial Ti_3Ni_4 particles exist in the interior of the martensite plate.

In conclusion, we can deduce that the deformation mechanism of aged $\text{Ti}_{49}\text{Ni}_{51}$ alloy under high-velocity impact is stress-induced martensite rather than a mixture of stress-induced martensite and dislocation generation. This is different from our previous study of high-velocity impacted $\text{Ti}_{50}\text{Ni}_{50}$ alloy [18]. It may be because the Ti_3Ni_4 dispersed uniformly in the matrix and enhanced the strength of the matrix that dislocation is difficult to introduce.

As the distance increases from the crater, the volume fraction of the martensite plates reduces due to the decrease in the material stress, strain, strain rate and degree of deformation, as shown in Figure 5a–f. When the distance from the crater is 5–6 mm, the microstructure is similar to that of non-impact. In short, the transformation behavior and microstructure along the impact direction after high-velocity impact emerge with regionalization characteristics; the bottom of the crater was classified into a deformed region near the crater (0–4 mm) and an un-deformed region of the distal crater (5–6 mm).

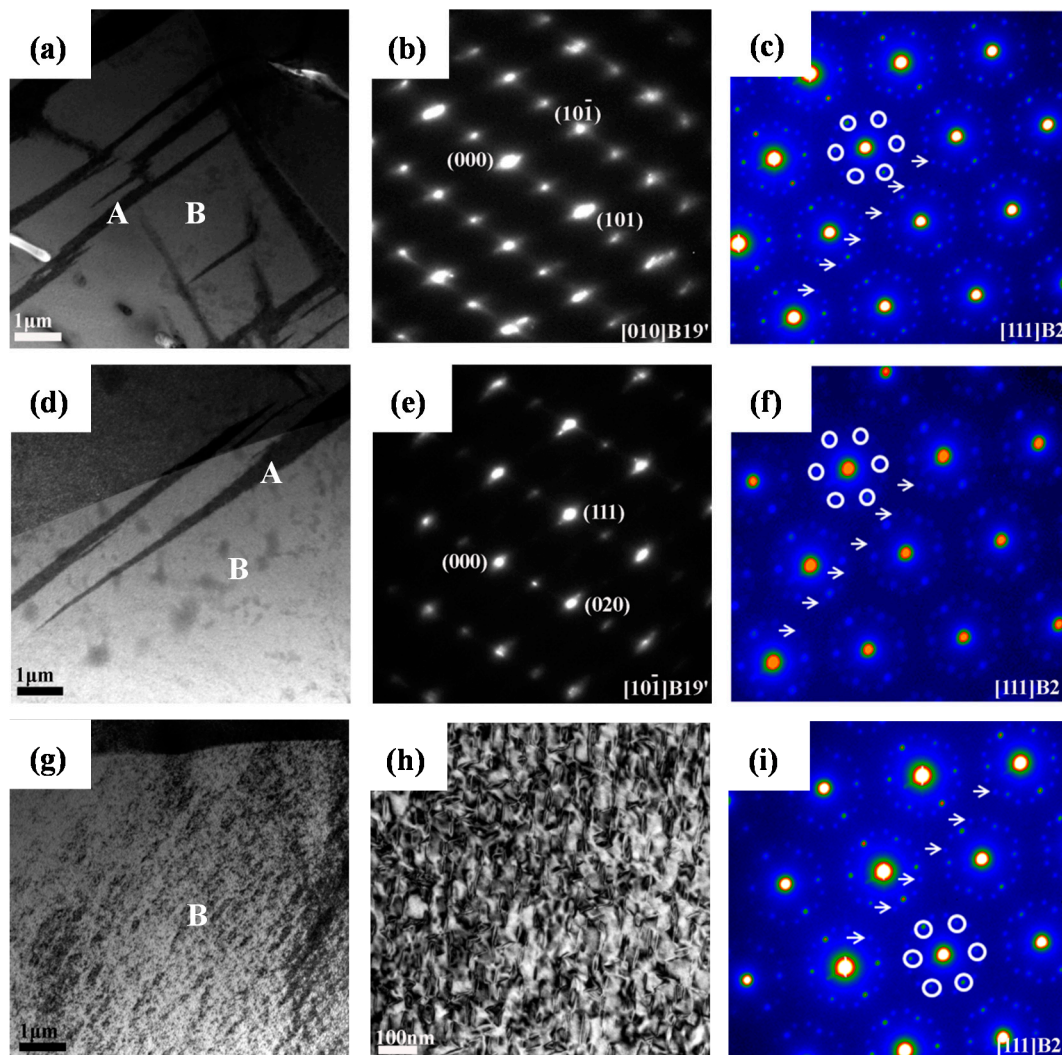


Figure 5. TEM micrographs and SAED patterns of aged $\text{Ti}_{49}\text{Ni}_{51}$ alloy after impact: (a) Bright-field image of 1 mm; (b) SAED pattern of area A in (a); (c) SAED pattern of area B in (a); (d) Bright-field image of 2–4 mm; (e) SAED pattern of area A in (d); (f) SAED pattern of area B in (d); (g) Bright-field image of 5–6 mm; (h) Magnified microstructures of area B in (g); (i) SAED pattern of area B in (g).

Figure 6 shows the microhardness of aged $\text{Ti}_{49}\text{Ni}_{51}$ alloy before and after impact. The microhardness for solution-treated $\text{Ti}_{49}\text{Ni}_{51}$ alloy is ~ 240 under 300 g for 15 s, and the microhardness for aged $\text{Ti}_{49}\text{Ni}_{51}$ alloy before impact is ~ 300 . While the microhardness near the crater increased to ~ 380 , this may be because the material was subjected to the most severe plastic deformation during impact. Moreover, the microhardness decreased with the increasing distance from the crater due to the decrease in the material stress and degree of deformation. The microhardness of 4–6 mm from the crater approximates that of non-impact. Therefore, impact can achieve a gradient variation in the deformation degree from the bottom of the crater to the deep matrix.

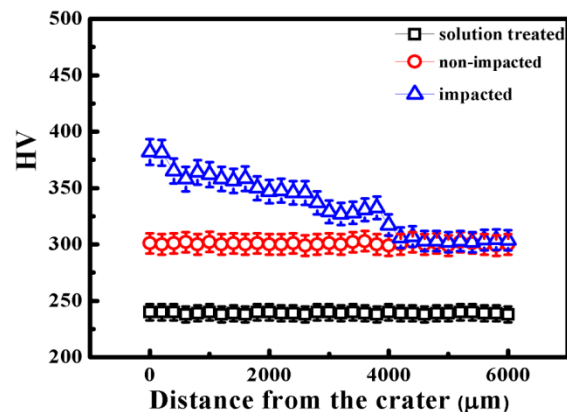


Figure 6. Microhardness distribution along crater in aged $\text{Ti}_{49}\text{Ni}_{51}$ alloy before and after impact.

4. Conclusions

The transformation behavior, microstructure and mechanical property of aged $\text{Ti}_{49}\text{Ni}_{51}$ alloy can achieve a regionalized variation from the bottom of the crater to the deep matrix. The generation of stress-induced martensitic transformation is due to the concentration of stress in the grain boundary, under the shock waves. The small change of dislocation density is because of the enhanced matrix strength due to Ti_3Ni_4 particles. The number of martensite plates and the microhardness reduce with the increasing distance from the crater.

Acknowledgments: This work is supported by Natural Science Foundation of China (No. 51571074, 51271066 and 51371069).

Author Contributions: Yingying Zhu conceived and designed the experiments; Yingying Zhu, Haizhen Wang performed the experiments; Yingying Zhu, Haizhen Wang, Zhiyong Gao analyzed the data; Yingying Zhu, Haizhen Wang, Zhiyong Gao and Wei Cai wrote the paper.

Conflicts of Interest: The authors declare no conflict of interest.

References

1. Takeda, K.; Matsui, R.; Tobushi, H. Transformation-induced relaxation and stress recovery of TiNi shape memory alloy. *Materials* **2014**, *7*, 1912–1926. [[CrossRef](#)]
2. Kim, J.I.; Liu, Y.N.; Miyazaki, S. Aging-induced two-stage R-phase transformation in Ti-50.9 at % Ni. *Acta Mater.* **2004**, *52*, 487–499. [[CrossRef](#)]
3. Kim, J.I.; Miyazaki, S. Effect of nano-scaled precipitates on shape memory behavior of Ti-50.9 at % Ni alloy. *Acta Mater.* **2005**, *53*, 4545–4554. [[CrossRef](#)]
4. Chang, S.H.; Wu, S.K.; Chang, G.H. Grain size effect on multiple-stage transformations of a cold-rolled and annealed equiatomic TiNi alloy. *Scr. Mater.* **2005**, *52*, 1341–1346. [[CrossRef](#)]
5. Nazarenko, A.I. Technique and some results of space debris penetration probability estimate for Russian modules of ISS. In Proceedings of the 17th IADC Meeting, Darmstadt, Germany, 11–13 October 1999.
6. Filip, P.; Mazanec, K. On precipitation kinetics in TiNi shape memory alloys. *Scr. Mater.* **2001**, *45*, 701–707. [[CrossRef](#)]

7. Jafar, K.A.; Antonin, D.; Gunther, E. Ni₄Ti₃-precipitation during aging of NiTi shape memory alloys and its influence on martensitic phase transformations. *Acta Mater.* **2002**, *50*, 4255–4274.
8. Fatemeh, K.; Jafar, K.A.; Vahid, A.C. Effect of short-time annealing treatment on the superelastic behavior of cold drawn Ni-rich NiTi shape memory wires. *Alloys Compd.* **2013**, *554*, 32–38.
9. Zhou, Y.; Fan, G.; Zhang, J.; Ding, X.; Ren, X.; Sun, J.; Otsuka, K. Understanding of multi-stage R-phase transformation in aged Ni-rich Ti-Ni shape memory alloys. *Mater. Sci. Eng. A* **2006**, *438–440*, 602–607. [[CrossRef](#)]
10. Liu, H.T.; Sun, G.A.; Wang, Y.D. Shock-induced transformation behavior in NiTi shape memory alloy. *Acta Phys. Sin.* **2013**, *62*, 018103.
11. Kurita, T.; Matsumoto, H.; Sakamoto, K. Transformation behavior of shock-compressed Ni₄₈Ti₅₂. *Alloys Compd.* **2005**, *400*, 92–95. [[CrossRef](#)]
12. Gao, C.; Dong, S.L. Damage Behaviors of AZ31 Magnesium Alloy and Zirconium 702 Induced by Hypervelocity Impact. Master's Thesis, Harbin Institute of Technology, Harbin, China, July 2013.
13. Zou, D.L.; Zhen, L.; Xu, C.Y. Characterization of adiabatic shear bands in AM60B magnesium alloy under ballistic impact. *Mater Charact.* **2011**, *62*, 496–502. [[CrossRef](#)]
14. Zhou, Y.M.; Zhang, J.; Fan, G.L.; Ding, X.D.; Sun, J.; Ren, X.B.; Otsuka, K. Origin of 2-stage R-phase transformation in low-temperature aged Ni-rich Ti-Ni alloys. *Acta Mater.* **2005**, *53*, 5365–5377. [[CrossRef](#)]
15. Fan, G.L.; Chen, W.; Yang, S.; Zhu, J.H.; Ren, X.B.; Otsuka, K. Origin of abnormal multi-stage martensitic transformation behavior in aged Ni-rich Ti-Ni shape memory alloys. *Acta Mater.* **2004**, *61*, 4351–4362. [[CrossRef](#)]
16. Xu, G.L.; Wang, C.Y.; Beltrán, J.I.; LLorca, J.; Cui, Y.W. Landau modeling of dynamical nucleation of martensite at grain boundaries under local stress. *Comput. Mater. Sci.* **2016**, *118*, 103–111. [[CrossRef](#)]
17. Zhang, X.N.; Xia, B.Y.; Chen, J.; Song, B.; Tian, X.L.; Hao, Y.M.; Xie, C.Y. Effects of equal channel angular extrusion and aging treatment on R phase transformation behaviors and Ti₃Ni₄ precipitates of Ni-rich TiNi alloys. *Alloys Compd.* **2011**, *509*, 6296–6301. [[CrossRef](#)]
18. Zhu, Y.Y.; Wang, H.Z.; Gao, Z.Y.; Cai, W. Phase transformation and mechanical properties of Ti₅₀Ni₅₀ alloy after high-velocity impact. *Alloys Compd.* **2016**, *664*, 223–228. [[CrossRef](#)]



© 2016 by the authors; licensee MDPI, Basel, Switzerland. This article is an open access article distributed under the terms and conditions of the Creative Commons Attribution (CC-BY) license (<http://creativecommons.org/licenses/by/4.0/>).